PAPER

Check for updates

Reusable magnetic mixture of CuFe$_2$O$_4$–Fe$_2$O$_3$ and TiO$_2$ for photocatalytic degradation of pesticides in water†

Dmytro Danilian, [iD] *[a] Franziska Maria Bundrück,[a] Arvo Kikas,[a] Tanel Käämbre,[a] Hugo Mändar,[a] Sandro Lehner,[b] Alexander Gogos, [iD] [cd] Jekaterina Kozlova,[a] Mati Kook,[a] Valter Kiisk,[a] Joosep Link,[e] Raivo Stern, [iD] [e] Angela Ivask, [iD] [f] Vambola Kisand [iD] *[a] and Rainer Pärna [iD] [a]

Photocatalysis is a promising treatment method to remove pollutants from water. TiO$_2$-P25 is a commercially available model photocatalyst, which very efficiently degrades organic pollutants under UVA light exposure. However, the collection and the recovery of TiO$_2$-P25 from cleaned water poses significant difficulties, severely limiting its usability. To address this challenge, we have prepared a sintered mixture of TiO$_2$-P25 nanomaterials and magnetic CuFe$_2$O$_4$–Fe$_2$O$_3$ nanocomposites. The mixture material was shown to contain spinel ferrite, hematite and maghemite structures, copper predominantly in Cu^{2+} and iron predominantly in Fe^{3+} state. The CuFe$_2$O$_4$–Fe$_2$O$_3$ and TiO$_2$-P25 mixture demonstrated magnetic collectability from processed water and photocatalytic activity, which was evidenced through the successful photodegradation of the herbicide 2,4-D. Our findings suggest that the sintered mixture of CuFe$_2$O$_4$–Fe$_2$O$_3$ and TiO$_2$-P25 holds a promise for improving photocatalytic water treatment, with the potential to overcome current photocatalyst recovery issues.

1 Introduction

Pesticides are chemical compounds that are used in increasing quantities to inhibit the growth or survival of unwanted organisms. Due to their extensive application on soil but also spills and disposal, pesticides may accumulate in different environmental compartments.[1] This can lead to contamination of surface water or groundwaters.[2] A recent study in Estonia[3,4] has demonstrated that both in the water table and in borehole wells, the level of pesticides can exceed the respective regulatory threshold values indicating that pesticide-polluted water,

particularly in agricultural and rural areas, may pose a potential health hazard.[5]

In order to overcome the limitations of more conventional water purification procedures at large-scale facilities several new local drinking water treatment technologies (*e.g.*, ozone, ultraviolet, silver ion, ferrate) have been recently developed.[6,7] As a promising approach for water treatment, photocatalysis stands out for its innovative potential.[8–12] Photocatalysis is a process facilitating light-induced modification of a substance. Therefore, photocatalyst materials can often be useful in transforming harmful pollutants into harmless substances under sunlight. Currently, photocatalytic degradation of harmful organic pollutants can be realistically applied to small to medium size water purification setups, once sufficient efficiency of the process as well as recyclability of the photocatalyst materials are ensured.[13–15] An important determinant is also non-toxicity of the reaction end-products, especially when photocatalytic degradation concerns phenolic pollutants.[16]

During the last three decades, titania (TiO$_2$) has attracted much attention as a robust high-efficiency solar light activated photocatalyst material. However, due to its rather large band gap, TiO$_2$ absorbs only a fraction of sunlight. Its band gap depends on crystal structure and is typically 3.2 eV in the case of anatase and 3.0 eV in the case of rutile, which means it can only use a small part of the solar spectrum. Evonik Aeroxide P25 (formerly Degussa P25) is a flame-made multiphasic TiO$_2$ nanoparticle powder containing anatase and rutile. The past

[a]Institute of Physics, University of Tartu, W.Ostwaldi 1, Tartu 50411, Estonia. E-mail: vambola.kisand@ut.ee; dmytro.danilian@ut.ee

[b]Laboratory of Advanced Fibers, Department of Materials Meet Life, Swiss Federal Laboratories for Materials Science and Technology (Empa), Lerchenfeldstrasse 5, St. Gallen 9014, Switzerland

[c]Laboratory for Particles-Biology Interactions, Department of Materials Meet Life, Swiss Federal Laboratories for Materials Science and Technology (Empa), Lerchenfeldstrasse 5, St. Gallen 9014, Switzerland

[d]Nanoparticle Systems Engineering Laboratory, Institute of Energy and Process Engineering (IEPE), Department of Mechanical and Process Engineering (D-MAVT), ETH Zurich, Sonneggstrasse 3, Zurich 8092, Switzerland

[e]National Institute of Chemical Physics & Biophysics, Akadeemia tee 23, 12618, Tallinn, Estonia

[f]Institute of Molecular and Cell Biology, University of Tartu, Riia 23, 51010 Tartu, Estonia

decades have witnessed the wide applications range of P25 as a benchmark material for studying photocatalytic mechanisms, materials, and processes.[13] However, the photocatalytic efficiency of TiO_2 is restricted by several factors, such as limited absorption in the solar spectrum, short lifetime of photo-generated electrons, and poor collectability after its use.[13] Therefore, different methods have been proposed to improve the performance of TiO_2. One of such changes involves combination of TiO_2 with other oxide semiconductors,[17,18] which is expected to contribute both to the increased photocatalytic performance as well as to collectability and therefore, improved reusability.

One viable option to improve the collectability of photocatalytic materials is to supply them with magnetic properties. One known magnetic photocatalyst is ferrimagnetic maghemite (γ-Fe_2O_3).[19] However, maghemite is a material with relatively low stability. The most common form of Fe_2O_3, hematite (α-Fe_2O_3) is a stable material with fairly narrow bandgap (2.2 eV), but with very weak magnetic moment due to its canted anti-ferromagnetic order.[20] In addition to poor magnetic properties, hematite has particularly rapid recombination of the photo-generated charge carriers, which critically limits its photocatalytic potential.[21,22] A promising strongly magnetic photocatalytic material with high magnetic stability near room temperature (Curie temperature as high as $\sim$750 K) is $CuFe_2O_4$.[23] Compared with binary iron oxide-based materials, this material can be seen as potentially more robust against photocorrosion or oxidative changes at ambient conditions as it does not contain ferrous iron (like magnetite) and does not depend on vacancies in structure (like maghemite), both of which tend to lead to fully oxidized stable hematite phase in an oxidative environment. $CuFe_2O_4$ material has an even smaller band gap value ($\sim$1.6 eV) than iron oxide materials but again, its photocatalytic efficiency is limited due to charge recombination, inherent for the strong light absorbance, small band gap materials.[23] Therefore, currently according to our knowledge, there is no material with sufficient photocatalytic activity and decent magnetic collectability.

In this study, we propose a combination of TiO_2 and α-Fe_2O_3 with $CuFe_2O_4$ to design magnetically collectable photocatalyst material.

Coprecipitation method was used to synthesize $CuFe_2O_4$–Fe_2O_3 material with controlled particle size distribution. The synthesized $CuFe_2O_4$–Fe_2O_3 was then mechanically mixed with TiO_2-P25, the mix was annealed at 600 °C to allow particles to sinter and form enduring mechanical contact. Finally, the nonmagnetic (titania) particles that had not attached to any magnetic material were excluded by using a strong permanent magnet to lift and collect the particle agglomerates that contained magnetic components. The composition of the obtained material was characterised using multiple analytical methods. The functionality of the material was assessed by measuring the photocatalytic degradation rate of aqueous 2,4-dichlorophenoxyacetic acid (2,4-D) solution as a model for a commonly used pesticide for weed control.[24] We demonstrate that the sintered mixture of $CuFe_2O_4$–Fe_2O_3 and TiO_2-P25 can be magnetically collected from water solution and reused as

a sustainable and effective method for pesticide removal from drinking water.

2 Experimental

2.1 Synthesis of materials and magnetic extraction

The $CuFe_2O_4$–Fe_2O_3 was synthesised using a co-precipitation method. The precursor reagents $Cu(NO_3)_2 \times 3H_2O$ (99% purity, trace metals based), the $Fe(NO_3)_3 \times 9H_2O$ (99% purity, trace metals based) and NH_4OH (98% purity) were all obtained from Sigma-Aldrich. The salts were dissolved in deionised (DI) water (8.7 MΩ cm) to produce solution containing 0.01 M $Cu(NO_3)_2 \times 3H_2O$ and 0.02 M $Fe(NO_3)_3 \times 9H_2O$ to which a 3.34 M aqueous solution of NH_4OH was added dropwise until the pH of the solution reached approximately 11 and the precipitation was complete. The obtained precipitate was washed with DI water five times. Between every wash cycle, the precipitate was left at rest to settle for 15 minutes. Approximately 70% of the total liquid was carefully discarded at each wash cycle. To separate the precipitate from the remaining solution, centrifugation was performed at 2000 rpm for 5 minutes. Obtained precipitates were dried at a temperature of 60 °C for 12 hours. The dried powder was then annealed at 700 °C for 4 hours.

To obtain TiO_2-P25 with 20 wt% of $CuFe_2O_4$–Fe_2O_3, designated as TCF20-Sc (see ESI Table S1†), the annealed $CuFe_2O_4$–Fe_2O_3 powder was manually mechanically mixed with TiO_2 (Evonik Aeroxide P25, formerly Degussa P25) in 20 : 80 weight ratio using mortar and pestle, for a duration of 30 minutes. The resulting powder mixture was then subjected to additional annealing for 24 hours at 600 °C.

The process of magnetic extraction of the photocatalyst powder was carried out using a NdFeB N45-grade magnet of 20 kg pull force (dimensions 30 mm diameter and 10 mm height). The powder was positioned on a plastic weighing dish approximately 20 mm below a borosilicate glass barrier completely covering the surface area of a plastic weighing dish, then the magnet was placed above the borosilicate barrier. The magnet attracted powder from down to up onto the borosilicate barrier, separating it from weak/non-magnetic particles. Next, the plastic dish with initial material was changed to an empty one, and the magnet was carefully removed from above the barrier, allowing the magnetically separated powder to fall into the new plastic weighing dish. This separation process was repeated five times. As a result, from the initial mass approximately 40–50% was identified as having weak or non-magnetic properties. This portion was designated as "non-magnetic", referenced as TCF-NM. Adversely, the magnetically extracted fraction of TCF20-S material was designated as TCF-M. The TCF-M material, which has been recycled five times and subsequently characterised, was designated as TCF-M-5c. We note that the 20 : 80 wt% ratio of P25 and $CuFe_2O_4$–Fe_2O_3 in the ready mixture only applies for TCF20-S. After magnetic separation the respective ratios for TCF-NM and TCF-M were different.

As reference materials, TiO_2 (Evonik Aeroxide P25) and the same TiO_2-P25 annealed at 600 °C (referred as TiO_2-P25 @ 600 °C in text) were used. The latter provides a reference to possible

Paper

RSC Advances

changes in TiO_2 component itself when the mixtures were later annealed at similar temperature in order to achieve mechanically robust attachment of the Cu/Fe oxide to the titania particles.

2.2 Material characterisation

2.2.1 STEM/HAADF. The synthesised materials were characterised by Scanning Transmission Electron Microscopy (STEM) and Energy Dispersive X-ray (EDX) analysis to gain information on the microstructural features and elemental distribution. Samples were prepared by mixing a spatula tip of the respective dry powder with 300 μL ethanol (>99.9%, LiChrosolve, Supelco) in an Eppendorf tube. The sample was then sonicated for 2 min and left to sediment for 1 min. A volume of 10 μL from the supernatant was then drawn through a holey carbon nickel grid. After drying, most of the materials were analysed on a Talos F200× STEM (Thermo Fisher Scientific) and TCF-M-5c material by Titan Themis 200 (FEI) STEM equipped with the SuperX EDX system, both operated at an accelerating voltage of 200 kV. High-Angle Annular Dark-Field (HAADF) STEM images were obtained in conjunction with EDX elemental maps. Data was processed using the software Velox (Version 3.0.0.815, Thermo Fisher Scientific).

2.2.2 XRD. X-ray diffraction (XRD) patterns were recorded on diffractometer SmartLab™ (Rigaku, Japan) implementing Bragg–Brentano optical geometry and CuKα radiation (wavelength 0.154 178 nm) from rotating anode working at 8.1 kW (45 kV and 180 mA). Powder diffraction database PDF-2 (version 2023) was used for qualitative analysis of phases. Rietveld analysis (program TOPAS 6) was used for a rough estimation of concentrations of the phases.

2.2.3 Raman microscopy. Raman spectra of the materials were acquired by using a Raman microscope (inVia, Renishaw, UK) at ambient temperature. The powders were deposited onto a silicon wafer, 514.5× nm emission argon-ion laser was used for excitation and 50× objective was used to focus the laser beam and collect the backscattered light. The incident power was typically kept at 1 mW along with a slight defocusing of the beam (spot size ∼10 μm) to avoid any photoinduced damage to the sample. The spectral resolution of the Raman microscope was approximately 2 cm^{-1}.

2.2.4 ICP-OES. Elemental contents of the materials were quantitatively assessed by using Inductively Coupled Plasma Optical Emission Spectroscopy (ICP-OES). To this end, ≈10 mg of dry powder was mixed with 3 ml HNO_3 (69%), 1 ml H_2O_2 (30%), and 1 ml HF (40%) and digested using a pressurised microwave (Ultraclave, MLS GmbH, Germany) at 240 °C and 100 bar for 10 min. After the digestion process, the mixture was brought till 50 ml using ultrapure water and analysed using Agilent 5110 ICP-OES. The elements were quantified using external calibration with the respective certified aqueous standards (Inorganic ventures). The limit of quantification (LOQ) for each element was determined from procedure blanks (a material that contains everything except for the analyte of interest) according to LOQ = x_{BL} + ($9\sigma_{BL}$), where x_{BL} is the average concentration of the elements in the procedure blanks and σ_{BL}

is the corresponding standard deviation. The LOQs were 2.3 μg L^{-1} for both Ti and Cu and 26 μg L^{-1} for Fe.

2.2.5 XPS. X-ray Photoelectron Spectroscopy (XPS) experiments with materials were conducted using an electron energy analyser (SCIENTA SES 100) and a non-monochromatic twin anode X-ray tube (Thermo XR3E2). The X-ray tube had characteristic energies of 1253.6 eV (Mg Kα 1,2 FWHM 0.68 eV) and 1486.6 eV (Al Kα 1,2 FWHM 0.83 eV). All XPS measurements took place in Ultra-High Vacuum (UHV) conditions with a pressure of less than 5×10^{-9} mbar. The angle between the analyser and the X-ray source was 45°. The binding energy scales for the XPS experiments were referenced to the binding energy of the C 1s photoemission line, 284.8 eV. The raw data obtained from the experiments were processed using the software Casa XPS version 2.3.23.[25] The processing steps involved the removal of Kα and Kβ satellites, as well as fitting the components. The Shirley background was used and a Gauss–Lorentz hybrid function (GL70, Gauss 30%, Lorentz 70%) was employed for fitting the components, ensuring the best fit.

2.2.6 NEXAFS. Near Edge X-ray Absorption Fine Structure (NEXAFS) measurements were conducted at the solid-state endstation of the FinEstBeaMS of MAX-IV synchrotron.[26,27] The NEXAFS measurements were performed in the total electron yield mode by monitoring the sample drain current using ALBA electrometer.[26] The sample current signal was normalised to the incoming flux (simultaneously) measured using the photocurrent signal from a clean gold mesh positioned between the material and the last optical element of the beamline.

2.2.7 UV-vis absorbance. Material absorbance measurements were determined by measuring diffused reflectance using UV-visible spectrophotometer equipped with a tungsten lamp and a photomultiplier (Agilent Cary 5000 UV-Vis-NIR, USA). Material was measured in a powder cell (22 mm diameter a quartz window with maximum volume 1 cm^3). Polytetrafluoroethylene (PTFE) signal was used as a baseline for diffuse reflectance spectroscopy and spectral resolution was 0.1 nm. Measured diffuse reflectance spectra are transformed to the absorption spectra using an equation $A = 2 + \log(1/R)$, where A is absorbance, R is reflectance of material[28] and 2 is normalization coefficient.

2.2.8 Magnetic characterisation. Magnetic properties of the materials were measured with Physical Property Measurement System (PPMS 14 T, Quantum Design, USA). Measurements at and below room temperature were conducted with the Vibrating Sample Magnetometer (VSM) option and the powdered materials were enclosed in appropriate nonmagnetic plastic capsules. High temperature measurements were performed with the VSM OVEN option and materials were attached to the OVEN measurement stick mixed in a drop of recommended Zircar cement. High temperature measurements were scaled to low temperature measurements at the overlapping temperature of 300 K. Magnetic field up to 20 k Oe (2 T) was used to record the hysteresis in magnetic isotherms. Magnetic flux trapping in PPMS superconducting solenoid is accounted for and reported magnetic field is corrected using a Pd standard following the recommended procedure.[29] A small magnetic field of 100 Oe (0.01 T) was applied during temperature dependent

measurements and magnetic transition temperatures were determined from the extrema in temperature derivative dM dT^{-1}.

2.2.9 Photocatalytic evaluation. Photocatalytic activity of the materials was evaluated through degradation of 10^{-4} M solution of 2,4-D (PESTANAL, Sigma-Aldrich, purity $\geq$ 98.0%) in DI water. The concentration 0.1 mM of 2,4-D was above environmental levels, but this was chosen to ensure detectable photocatalytic kinetics. Degradation of 2,4-D was measured during 18 h illumination under a custom-assembled lamp, equipped with four 15 W iSOLde Cleo fluorescent Hg light bulbs (λ_{max} = 355 nm). The measured light intensity of this lamp in 315–400 nm spectral range at the test surface height ranged between 2.8 and 3.2 W m^{-2}, as determined using a Delta Ohm UVA probe. Quartz cuvettes were chosen as the measurement vessels. Each cuvette contained 3.5 ml of the 2,4-D solution. To achieve the final concentration of 1 mg ml^{-1}, 3.5 mg of the analysed materials were added to each cuvette. For each material, the 2,4-D decay measurement was repeated 5 times. The cuvettes with 2,4-D were placed horizontally, and the materials were evenly distributed along one edge of the cuvettes without stirring. Before illumination, the mixtures were incubated for 30 min in the climate chamber (Memmert CTC 256, Germany)

at a temperature of 22.5 °C in the dark to enable adsorption of the pesticide to materials. Degradation of 2,4-D was measured using UV-vis spectrometer Agilent Cary 5000, within 400-200 nm every 30 min during 18 hours light illumination in the climate chamber. Absorbance intensity at 229 nm was used to evaluate 2,4-D degradation.

For repeated use, TCF-M material, post 2,4-D degradation, was reclaimed using a magnet, attracting the material to a borosilicate glass barrier. This recovered material was then thoroughly rinsed five times with DI and dried in an oven at 70 °C for 12 hours.

3 Results and discussion

3.1 Morphology of particles and element distribution

Distinct differences in particle morphology and element distribution were observed between TiO$_2$-P25 @ 600 °C, CuFe$_2$O$_4$–Fe$_2$O$_3$ materials and mixtures TCF20-S, TCF-NM, TCF-M, and TCF-M-5c (Fig. 1). STEM results indicate that TiO$_2$-P25 @ 600 °C particles agglomerated and exhibited higher polydispersity compared to the initial TiO$_2$-P25 material.[30] The relatively high polydispersity of TiO$_2$-P25 @ 600 °C (particle sizes approx. $\approx$200 nm down to tens of nm) can be seen from
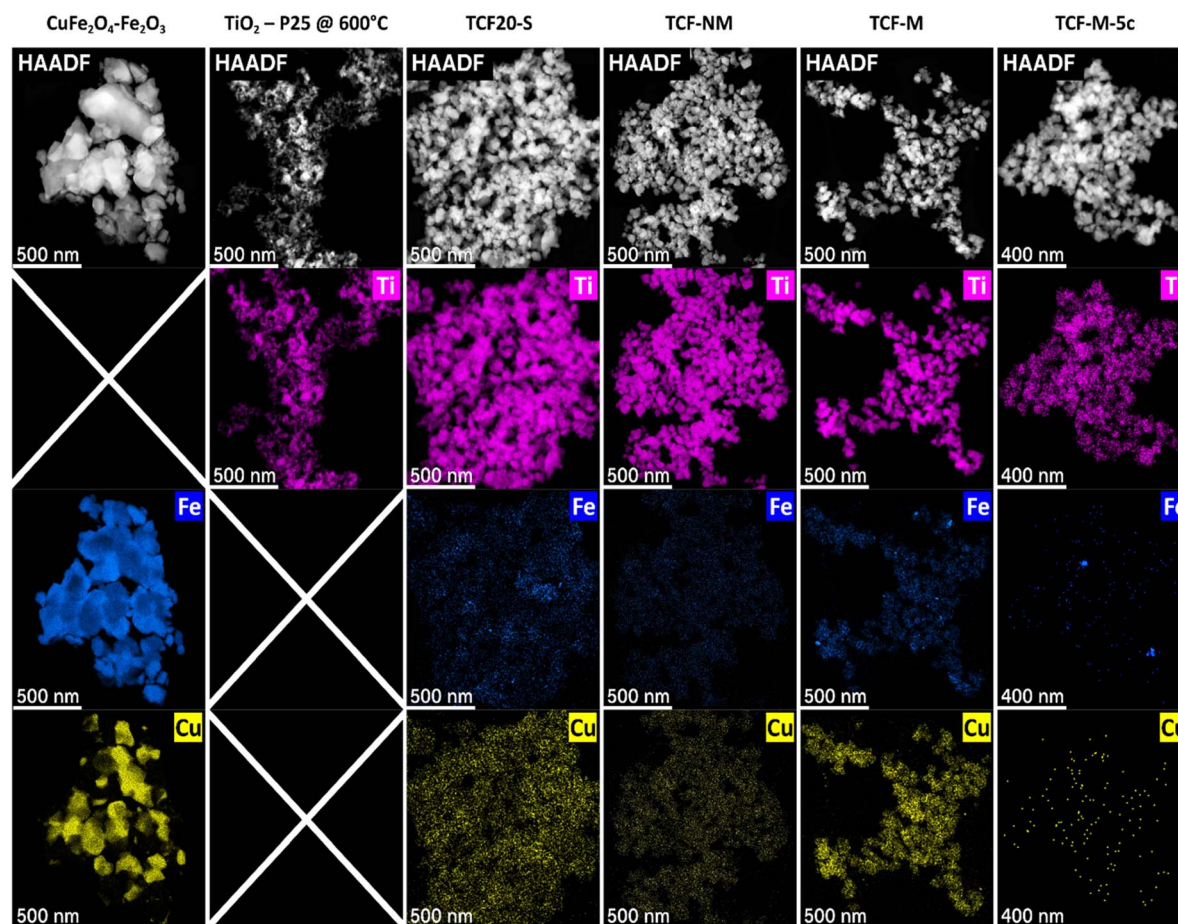

Fig. 1 STEM-HAADF micrographs along with corresponding elemental maps of CuFe$_2$O$_4$–Fe$_2$O$_3$, TiO$_2$-P25 @ 600 °C, TCF20-S, TCF-NM, TCF-M, and TCF-M-5c.

ESI Fig. S1†. Compared with TiO_2 materials, $CuFe_2O_4$–Fe_2O_3 showed significantly larger grain sizes (roughly 1 μm to ≈100 nm). However, the mixture materials TCF20-S, TCF-NM and magnetically extracted TCF-M all had similar grain size and morphology with respect to the TiO_2. STEM-HAADF (Fig. 1) indicated the presence of elements as expected from materials composition. In TiO_2-P25 @ 600 °C the predominant element was Ti while no Cu of Fe were detected. In all other materials, Fe and Cu signals were detected. Interestingly, copper appeared to be homogenously distributed in most of the materials, whereas Fe was observed in nanoscopic clusters with a size of a few nm. After magnetic extraction, both Fe and Cu were only barely detectable in the residual TCF-NM, suggesting successful magnetic removal of Fe rich material from TCF20-S. In contrast, the extracted magnetic fraction (TCF-M) appeared slightly richer in general Fe content as well as in nanoscopic Fe clusters throughout the material, while the distribution of Cu was uniform. The presence of Fe and Cu was also seen in the recycled material TCF-M-5c as seen both, from STEM-EDX maps (see Fig. 1 and ESI S2†) as well as from energy-dispersive X-ray spectra (see ESI Fig. S3†).
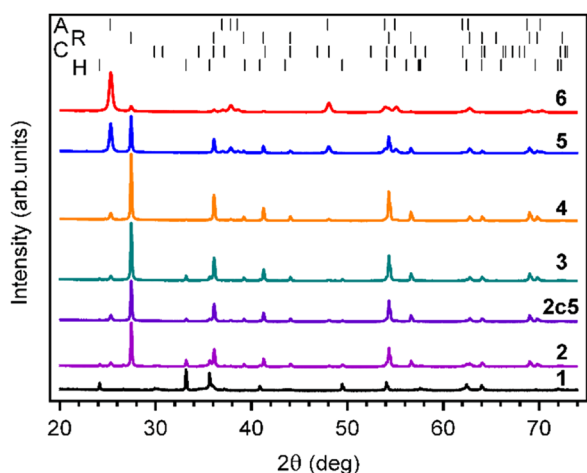

Fig. 2 XRD patterns of 1 – $CuFe_2O_4$–Fe_2O_3, 2 – TCF-M, 2c5 – TCF-M-5c, 3 – TCF20-S and 4 – TCF-NM, 5 – TiO_2-P25 @ 600 °C, 6 – TiO_2-P25. The positions of reflection of anatase (A), rutile (R), $CuFe_2O_4$ spinel (C) and hematite (H) are shown as vertical bars at the upper part of the figure.

3.2 Crystal phase composition

The crystal phase of the materials was characterized using XRD and Raman spectroscopy. According to XRD, pure commercial TiO_2-P25 without thermal treatment consisted predominantly of anatase with a smaller fraction of rutile, as expected (Fig. 2 and Table 1). Annealing the TiO_2-P25 at 600 °C for 24 h resulted in partial TiO_2 phase transformation from anatase to rutile. The anatase to rutile ratio in the annealed material was close to 1. Indeed, anatase to rutile phase transformation temperature is known to be in the temperature range from 600 to 900 °C.[31]

The XRD pattern of $CuFe_2O_4$–Fe_2O_3 demonstrated the presence of three major phases, hematite (α-Fe_2O_3), $CuFe_2O_4$ spinel and maghemite (γ-Fe_2O_3), along with minor phase such as α-SiO_2. The source of α-SiO_2 could be impurities in precursor materials (Table 1). The predominant phase in TCF20-S diffractograms (Fig. 2) was rutile. The other phases in this material were anatase, hematite, $CuFe_2O_4$ spinel, and maghemite. After magnetic extraction, the material TCF-M was composed of the same phases as the TCF20-S but with different weights. The TCF-M contained relatively more hematite, but especially $CuFe_2O_4$ spinel and maghemite phases. Thus, TCF-M contained magnetic phases in higher concentration compared to TCF20-S. The nonmagnetic leftover material (TCF-NM) displayed primarily rutile and anatase fractions, along with reduced hematite and traces of $CuFe_2O_4$ spinel and maghemite (Table 1). Those results strongly suggest that the process of magnetic extraction was efficient in selection of the desired TCF-M materials. XRD results of TCF-M-5c revealed consistent phase composition with TCF-M, but with slightly higher rutile and $CuFe_2O_4$, suggesting stability and minimal transformation after five recycling cycles. In addition to XRD, Raman spectroscopy was used to analyse the phase composition of materials (Fig. 3). Raman spectrum confirmed that in TiO_2-P25, Raman bands at 144 cm^{-1} (E_g), 399 cm^{-1} (B_{1g}), 513 cm^{-1} (A_{1g}), 519 cm^{-1} (B_{1g}) and 640 cm^{-1} (E_g) related to anatase phase, were present.[32,33] In case of TiO_2-P25 @ 600 °C additional bands at 447 cm^{-1} (E_g) and 612 cm^{-1} (A_{1g}) related to rutile phase were detected.[34]

Interpretation of Raman spectrum of $CuFe_2O_4$–Fe_2O_3, TCF20-S, TCF-NM, TCF-M and TCF-M-5c (Fig. 3) was not quite straightforward due to overlapping peaks. We assigned the observed Raman bands at 219 cm^{-1}, 283 cm^{-1}, 397 cm^{-1}, 491 cm^{-1} and 600 cm^{-1} to hematite[35] and $CuFe_2O_4$.[23] Our

Table 1 Phase distribution and composition of pure TiO_2-P25, TiO_2-P25 @ 600° (24 h), $CuFe_2O_4$–Fe_2O_3, TCF20-S, TCF-NM, TCF-M and TCF-M-5c deduced from XRD data. R'_{wp} is the background excluded weighted residual error (R-factor) from Rietveld analysis.[38] The phases marked with "–" have shown concentrations with a low or under detection limit value (<0.2 wt%)

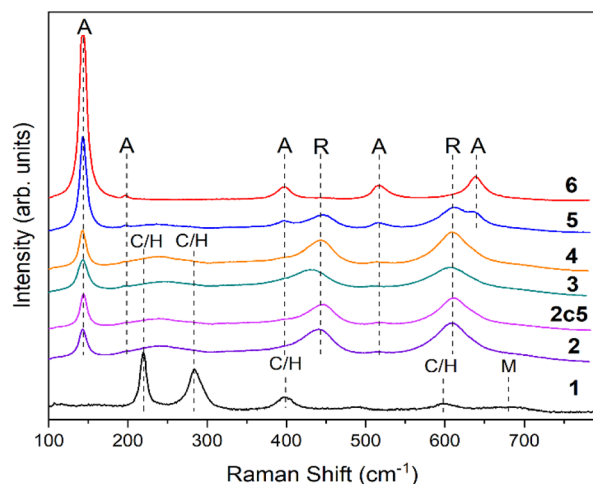| Material | Crystal phase, wt% | | | | | | |
	Anatase	Rutile	α-Fe_2O_3	$CuFe_2O_4$	α-SiO_2	γ-Fe_2O_3	R'_{wp}%
$CuFe_2O_4$–Fe_2O_3	—	—	53.5	33.9	1	11.6	13.7
TiO_2-P25	88.9	11.1	—	—	—	—	10.3
TiO_2-P25 @ 600 °C	51	49	—	—	—	—	7.7
TCF20-S	6.3	84.5	5.7	2.6	0.3	0.6	6.3
TCF-NM	10.8	87.2	0.9	0.5	0.2	0.4	6.1
TCF-M	6.7	69.6	12.4	8.8	1	1.5	7.2
TCF-M-5c	6.3	88.4	5.7	3.2	0.4	—	6.4

Fig. 3 The Raman spectra of 1 – $CuFe_2O_4$–Fe_2O_3, 2 – TCF-M, 2c5 – TCF-M-5c, 3 – TCF20-S, and 4 – TCF-NM, 5 – TiO_2-P25 @ 600 °C, 6 – TiO_2-P25. Dashed lines and capital letters present the positions of TiO_2 anatase (A), TiO_2 rutile (R), $CuFe_2O_4$ (C) or α-Fe_2O_3 (hematite, H) bands and γ-Fe_2O_3 (maghemite, M).

interpretation is based on previous findings, where Raman active modes of α-Fe_2O_3 (tetragonal crystal symmetry) have been detected at 225, 280, 400, 480, 615, and 690 cm^{-1}.[36] The Raman active mods of $CuFe_2O_4$ spinel have been detected at 215, 278, 481, 586, and 656 cm^{-1}, which are assigned to $F_{2g(1)}$, E_g, $F_{2g(2)}$, $F_{2g(3)}$, and A_{1g} modes, respectively.[36] The wide band at 680 cm^{-1} can be related to maghemite.[35] Raman bands of TCF20-S, TCF-NM, TCF-M and TCF-M-5c were mostly related to rutile with minor contribution to anatase. However, the materials demonstrated a wide Raman band at ∼260 cm^{-1}, which arises due to multiphonon process in rutile.[37]

3.3 Elemental composition

The elemental analysis of the $CuFe_2O_4$–Fe_2O_3 material confirmed the expected composition of the copper-iron oxide system (Table 2). The molar calculations, derived from the ICP-OES data, indicated a ∼6 : 1 ratio of iron to copper, in line with the presence of (binary) iron oxides as indicated by the XRD analysis (see Section 3.2) and the magnetisation measurements (see Section 3.7). This Fe : Cu ratio of ∼6 : 1, which roughly corresponds to 1 : 2 spinel : hematite molar ratio ($CuFe_2O_4$ molar mass is 239.1 amu, Fe_2O_3 molar mass is 159.6 amu), was

found to be comparable after introduction of $CuFe_2O_4$–Fe_2O_3 into the TCF20-S mixture. Also, after mixing, Cu and Fe content decreased in neat proportion to each other and in correspondence to the intended composition of 80 wt% TiO_2 and 20 wt% spinel-hematite mixture. The relative amount of Cu + Fe in the TCF20-S mixture closely corresponded to the expected value for the mixture of $CuFe_2O_4$–Fe_2O_3 (20% wt.) and TiO_2 (80% wt).

Upon the magnetic extraction, distinct compositional shifts were noted in the TCF-NM, and TCF-M samples compared with TCF20-S. Specifically, the TCF-NM sample exhibited a marked increase in the Ti/Fe ratio relative to TCF20-S, indicating that the nonmagnetic part remaining after extraction was mainly TiO_2. Conversely, the TCF-M material displayed a more balanced Ti and Fe distribution, indicative of successful incorporation of TiO_2 within the magnetic fraction. Recycled TCF-M-5c revealed similar atomic Fe/Cu ratio as a TCF-M.

These compositional findings align closely with our initial synthetic expectations, confirming the accuracy of our stoichiometric formulations. While slight variations were observed, they remained within the expected range of experimental and measurement precision. The ICP-OES analysis has thus provided a solid validation of the intended elemental makeup of our synthesized materials.

3.4 Composition of materials surface

To obtain information on elemental oxidation states of the very top layer of the materials' surface, XPS measurements were conducted. First of all, as expected, the XPS spectra of TiO_2-P25 @ 600° in the Fe 2p and Cu 2p region demonstrated only background noise (i.e. absence Fe and Cu impurities) and therefore is not presented in Fig. 1.

XPS spectra in Ti 2p region showed a spin–orbit doublet with peaks at 458.7 eV ($2p_{3/2}$) and 464.4 eV ($2p_{1/2}$) characteristic of Ti^{4+} oxidation state[39,40] for all materials containing Ti (Fig. 4a), as expected. No Ti^{3+} impurity contribution was found in any material, as shown (Fig. 4a). Fe $2p_{3/2}$ photoelectron peak (Fig. 4b) was observed at 710.8 eV in case of $CuFe_2O_4$–Fe_2O_3, with a satellite peak at 4.7 eV towards higher binding energies, indicating Fe^{3+} charge state. Based on Fe 2p binding energies in XPS spectra, it is inferred that the iron ions present in materials synthesised in $CuFe_2O_4$–Fe_2O_3 were in Fe^{3+} oxidation state.[41,42] No Fe^{2+} contributions were identified in Fe 2p spectra. This agrees with the XRD results, which indicated the presence of only Fe^{3+} compounds.

Table 2 ICP-OES analysis of elemental composition in $CuFe_2O_4$–Fe_2O_3, TCF20-S, TCF-NM, TCF-M and TCF-M-5c photocatalyst materials. wt% exceeding the sum of Cu, Fe and Ti is expected to be oxygen

| Material | wt% | | | | Atomic% (metals based) | | | | | (Cu + Fe) %at. |
	Cu	Fe	Ti	Sum (metals)	Cu	Fe	Ti	Fe/Cu (at.)	Ti/Cu (at.)	(metals based)
$CuFe_2O_4$–Fe_2O_3	11.97	62.47	0	73.43	14.5	85.5	0	5.9	0	100.0
TCF20-S	2.64	14.07	49.01	65.72	3.2	19.1	77.7	6	24.6	22.3
TCF-NM	0.42	2.45	55.82	58.69	0.55	3.6	95.8	6.6	175.8	4.2
TCF-M	6.75	33.42	30.89	71.07	7.9	44.3	47.8	5.6	6.1	52.2
TCF-M-5c	9.25	45.62	10.15	65.02	12.4	69.5	18.1	5.6	1.5	81.2

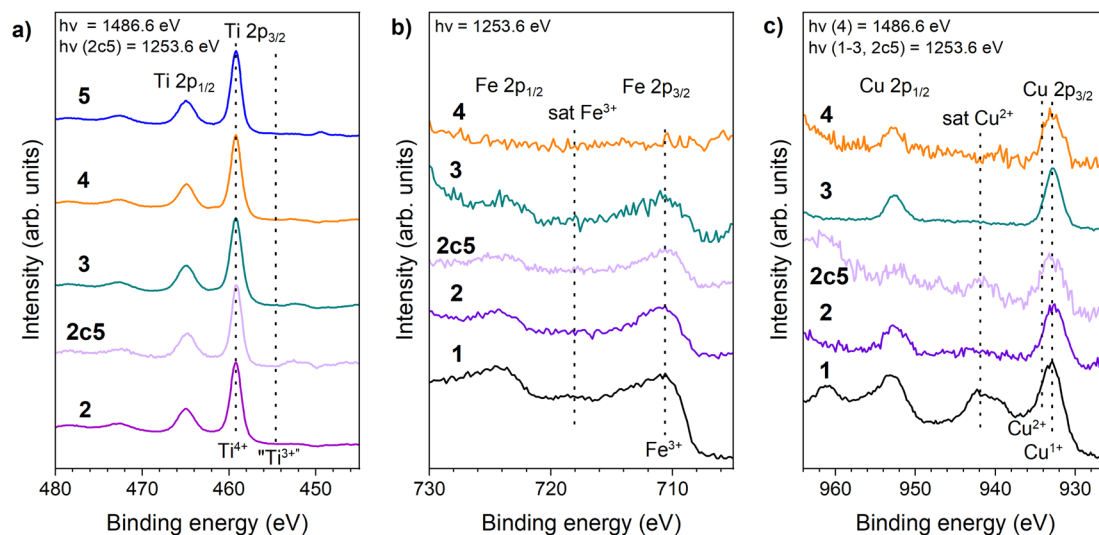Fig. 4 Photoelectron spectra of the Ti 2p region (a), Cu 2p region (b) and the Fe 2p region (c) of 1 − CuFe$_2$O$_4$–Fe$_2$O$_3$, 2 − TCF-M, 2c5 − TCF-M-5c 3 − TCF20-S, 4 − TCF-NM, 5 − TiO$_2$-P25 @ 600 °C.

Fe 2p spectra of mixed materials aligned with expectations (presence of Fe^{3+}), except for TCF-NM. This particular material uniquely demonstrated the absence of Fe 2p peaks, consistent with the anticipated outcome of the magnetic extraction process.

Cu 2p photoelectron spectra for all relevant samples are displayed in Fig. 4c. Cu 2p spectrum of pure CuFe$_2$O$_4$–Fe$_2$O$_3$ had Cu 2p$_{3/2}$ at 932.5 eV and Cu 2p$_{1/2}$ at 953 eV. The spectrum also showed a strong satellite line, characteristic of Cu^{2+},[43–45] as expected for Cu contained in ferrite. In the case of TCF20-S, TCF-NM, TCF-M and TCF-M-5c the spectra contained one photoelectron line per spin–orbit component with a weak shoulder at the higher binding energy side, and the (Cu^{2+}) satellite barely observable. Interestingly, XPS spectrum of TCF-M-5c illustrated a further diminished presence of the Cu^{2+} satellite features, suggesting a reduced intensity of Cu 2p compared to the material before its photocatalytic degradation cycles. This finding suggested the formation of Cu^{1+} at the surface of the material according to XPS.[44,46] However, this finding is contradictory to what XRD and Raman results demonstrated, as these did not indicate any phases related to Cu^{1+}. We therefore consider it plausible that the high Cu^{1+}/Cu^{2+} ratio we observe in XPS spectra is an effect of beam damage (reduction of Cu under irradiation of the XPS excitation source). Such 'beam damage' effect in Cu^{2+} compounds has been previously reported by others (e.g. in ref. 47 and 48) under varied excitation sources. We find such a scenario more plausible because we observed a slow degradation of the Cu^{2+} satellite intensity (relative to the main line) even when measuring the Cu 2p XPS of the TCF-M sample. Furthermore, the (relatively faster measurements of) Cu 2p NEXAFS of related samples (vide infra) all showed either pure or strongly dominant Cu^{2+} charge state.

Comparison of XPS spectra also indicates that the surface region (corresponding to the XPS probe depth of approximately 2 nm at the relevant kinetic energies[47]) is significantly more copper-rich (see ESI Table S2†) as compared to the bulk composition (viz. from ICP-OES). This suggests that the copper ferrite species is preferably concentrated at the surface of the nanoparticles, which from SEM information were estimated at ~20–100 nm in size.

3.5 Investigation of Cu and Fe chemical state

To further clarify the chemical state and local environment of Cu and Fe in CuFe$_2$O$_4$–Fe$_2$O$_3$ and TCF20-S, we carried out NEXAFS spectroscopic measurements of selected materials. The fine structure of Cu L$_{23}$ edge (see ESI Fig. S4†) revealed that copper is mainly in Cu^{2+} oxidation state in those materials and the fine structure of Fe L$_{23}$ edge showed that Fe is mainly present as Fe^{3+}. We note that NEXAFS provides a more sensitive tool as concerns the charge state of 3d metal ions than XPS (due to the continuum final state in the latter). NEXAFS measured in total electron yield (TEY) mode also has somewhat larger probe depth and is therefore less sensitive to surface impurities.[48] The NEXAFS results indeed do agree well with the analysis results of the XRD data where only Cu^{2+} compounds were identified.

Thus, we can conclude that X-ray irradiation during the lengthy (due to low signal level) XPS measurements may induce reduction of the Cu^{2+} to Cu^{1+} (Fig. 4c). This phenomenon has been also previously observed and reported.[49]

3.6 Optical absorption

The optical absorption spectra of all investigated materials are demonstrated in Fig. 5. Initially measured. In line with previous studies,[50] the absorption of TiO$_2$-P25 starts roughly at 400 nm. The absorption spectrum of synthesised black material of CuFe$_2$O$_4$–Fe$_2$O$_3$ covers evenly both the visible and UV range. It is in good accordance with previous investigations.[51] TCF20-S material exhibited intensive absorption in the UVA spectrum but also showed absorption in the visible light spectrum. Similar absorption profiles were observed for TCF-NM and TCF-M.
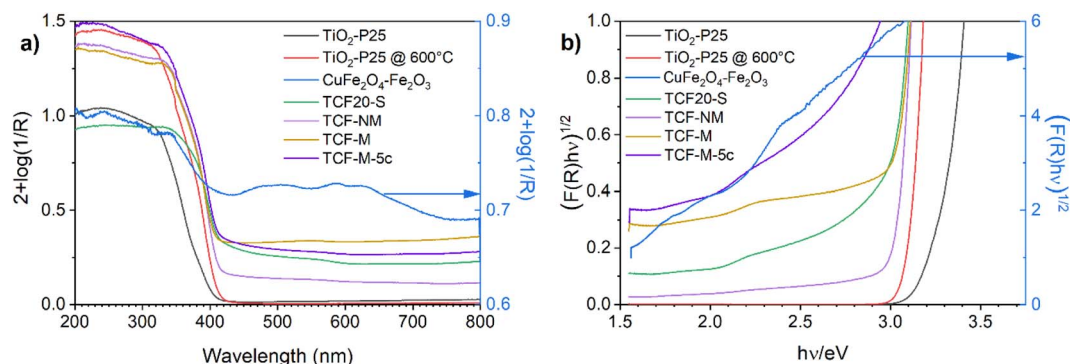
Fig. 5 The UV-vis absorption spectra of TiO$_2$-P25, CuFe$_2$O$_4$–Fe$_2$O$_3$, TCF20-S, TCF5-NM, TCF-M and TCF-M-5c materials. (a) Full spectra and (b) spectra plotted as $(F(R)(h\nu))^{1/2}$ *versus* photon energy graphs. Spectra for CuFe$_2$O$_4$–Fe$_2$O$_3$ (blue lines) are zoomed and respective *y*-axes on the right side are plotted blue.

Absorption edges of TCF20-S, TCF-NM, TCF-M and TCF-M-5c are shifted towards longer wavelengths compared with TiO$_2$-P25 (see Fig. 5a). The weak absorption at 560 nm is close to the band gap edge in hematite, maghemite and CuFe$_2$O$_4$.[40]

In order to estimate bandgaps from the diffuse reflectance data, the materials were analysed by using the Kubelka–Munk (K–M) theory from a plot $(F(R)(h\nu))^{1/2}$ *vs.* $h\nu$ (eV) where $F(R) = (1 - R)^2 (2R)^{-1}$ is K–M function and $h\nu$ is the photon energy in eV, as an intercept of the energy axis with a tangential straight line of the linear part of the graphs (Fig. 5b).[52] The absorption threshold values estimated from the Fig. 5b for the TiO$_2$-P25 (indirect optical bandgap) was 3.32 eV. TiO$_2$-P25 @ 600 °C material has an absorption threshold of 3.12 eV, which is due to the higher content of rutile in this material compared with TiO$_2$-P25. The CuFe$_2$O$_4$–Fe$_2$O$_3$ had several absorption thresholds, since it was composed of hematite, maghemite and CuFe$_2$O$_4$ spinel (Fig. 5b, blue line). The bandgap of hematite was 2.1 eV, which qualitatively agrees with an earlier theoretical estimate[53,54] TCF20-S had an absorption threshold of 2.97 eV, TCF-NM of 3.03 eV and TCF-M of 3.0 eV. The TCF20-S, TCF-M and TCF-M-5c had an additional absorption threshold at 2.1 eV, which was related to hematite. This result provides proof that materials absorb more visible light compared to pure TiO$_2$-P25.

3.7 Magnetic properties

The magnetic properties of the synthesised photocatalysts were analysed to probe the content of different magnetic phases. Further, it is also important to understand their behaviour under different magnetic fields, which is crucial to ensure robust magnetic collectability if proposed for real application in water treatment systems. These properties measured include bulk saturation magnetisation values, coercivity, and the critical temperatures (T_C).

The two materials with the strongest magnetic response were investigated (CuFe$_2$O$_4$–Fe$_2$O$_3$, TCF-M and TCF-M-5c). Table S3 (see ESI)† presents the magnetic properties of the prepared materials, with data including saturation magnetisation at 2 T, coercivity, and critical temperatures, as well as reference values from the literature for magnetic crystalline phases identified earlier by XRD.

For CuFe$_2$O$_4$–Fe$_2$O$_3$ material, the saturation magnetisation was recorded as 13.5 emu g^{-1}, and the coercivity was measured at 212 Oe. This material exhibited three distinct magnetic ordering temperatures at 859 K, 763 K, and 248 K, T_{C1}, T_{C2} and T_{C3} respectively (Fig. 6a).

In the case of TCF-M material, the saturation magnetisation at 2 T reduced to 6.12 emu g^{-1}. However, the coercivity increased to 428 Oe. The magnetic ordering temperatures for this material were observed at 852 K, 732 K, and 265 K. The analysis of TCF-M-5c demonstrated a significant alteration, notably the absence of the ~760 K transition, suggesting a phase composition change. This alteration, confirmed by the sole presence of the 844 K transition in both zero field cooled (ZFC) and field cooled (FC) magnetisation as well as derivative of FC line, aligns with XRD results indicating stability and subtle phase adjustments after multiple usage and recycling cycles.

Ordering at T_{C2} at around 731–763 K could be assigned to that of spinel ferrite CuFe$_2$O$_4$ with a known bulk Curie temp of 728 K.[57] The highest ordering temperature T_{C1} at 840–859 K would match well with $T_C = 858$ K of magnetite Fe$_3$O$_4$ (ref. 57) or, more plausibly (given the annealing parameters), maghemite.[55–59] We could not identify magnetite independently from the copper spinel from the XRD data with which it has almost overlapping reflexes (while for the same reason its presence cannot be ruled out). Although XRD confirms ferrimagnetic maghemite in CuFe$_2$O$_4$–Fe$_2$O$_3$ (11.6%) and in TCF-M (1.5% maghemite), its distinction from magnetite is more conclusively identified by magnetic analysis, specifically through the dM dT^{-1} measurements, given their overlapping XRD reflexes. Minute changes (on the order of 10 K) in this critical temperature together with the rather broad temperature range of the observed phase transition rather suggest the presence of both these phases with minor differences in their relative weights due to sample processing causing the apparent shift of the center of gravity of the transition. T_{C2} seemed to shift to slightly lower temperatures during repeated high temperature measurements and hysteresis at room temperature (Fig. 6b) changed slightly after the high temperature measurement procedure, further suggesting that the T_{C2} corresponds to
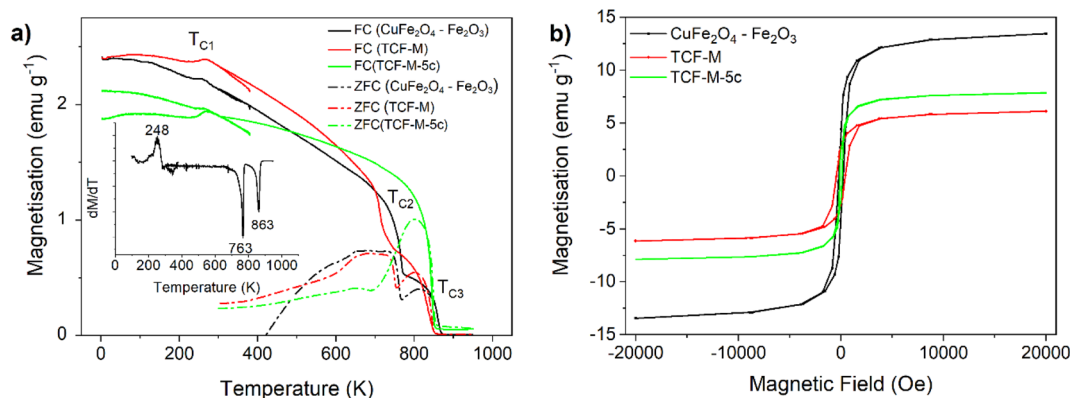
Fig. 6 The temperature dependence of the magnetisation (a) and the magnetization curves at room temperature (300 K) (b) of $CuFe_2O_4$–Fe_2O_3, TCF-M and TCF-M-5c materials. Initial zero field cooled (ZFC) and field cooled (FC) temperature dependencies reveal three magnetic transitions. The extrema in the temperature derivative curve dM dT^{-1} of the latter (Inset) are labelled by the estimates of the magnetic ordering temperatures in the $CuFe_2O_4$–Fe_2O_3 material.

ordering temperature of the metastable maghemite. Small decrease of magnetisation while cooling below ∼250 K at T_{C3} is assigned to the so-called Morin transition of hematite, below which hematite is perfectly antiferromagnetic and above a slightly canted antiferromagnet and thus possesses a weak magnetic moment.[57]

The measured saturation magnetization value can be compared to the weighted sum M_{sample} of the component magnetisations using the simple formula $M_{sample} = w_1 \times M_1 + w_2 \times M_2 + \ldots + w_n \times M_n$,[57] where w_i ($i = 1\ldots n$) are the weight fractions of all the phases derived from the XRD data and listed in Table 1 and M_i are the corresponding bulk magnetisation values from literature listed in Table S3.†[57] Based on phase composition, the measured magnetisation 13.5 emu g^{-1} at room temperature is comparable but slightly less than the calculated 17.5 emu g^{-1} value expected for the $CuFe_2O_4$–Fe_2O_3. In the case of TCF-M the recorded value of 6.12 emu g^{-1} is higher than the expected value of 3.39 emu g^{-1}. This analysis reaffirms the XRD findings, suggesting the magnetic characterization of TCF-M-5c reflects the noted phase stability and the observed decrease in Cu concentration, supporting the inference of slight compositional shifts post-recycling.

We conclude that magnetisation measurements provide a confirmation of the phase composition determined by XRD and even further removes some remaining ambiguity. Saturated magnetic moment at room temperature matches the value calculated by the weighted average of magnetisation of all phases reasonably well, at least in the order of magnitude level. All features of temperature dependence of magnetisation can be well explained by the Curie temperature of $CuFe_2O_4$, γ-Fe_2O_3/Fe_3O_4 and by Morin transition temperature of α-Fe_2O_3. The Néel temperature of α-Fe_2O_3 remained above the temperatures used during this study so was not experimentally confirmed.

3.8 Photocatalytic activity

Photocatalytic activity of pure TiO$_2$-P25, TiO$_2$-P25 @ 600 °C, $CuFe_2O_4$–Fe_2O_3, TCF20-S, TCF-NM and TCF-M measured as degradation of model herbicide pollutant 2,4-D is demonstrated

in Fig. 7. The performance of pure 2,4-D provided a baseline for comparison, indicating the potential decay of this mode pollutant under UVA light. According to our results, 2,4-D was rather stable under UVA and only slight (10%) degradation was observed after prolonged (18 h) irradiation. It is important to note that in our experimental set-up photocatalytic activity was measured without any stirring and with the studied materials placed on the surface of the 2,4-D solution. Such a set-up may result in lower photocatalytic activity than one would achieve with stirring. However, degradation of 2,4-D was well detectable with all the tested materials (see ESI Fig. S5†).

The photodegradation process of 2,4-D is relatively well described and involves transformation of 2,4-D into chlorinated intermediates and then into compounds like 1,2,4-benzenetriol and chlorohydroquinone, which undergo ring-opening and hydrolysis reactions catalysed by the TiO$_2$ surface, leading to
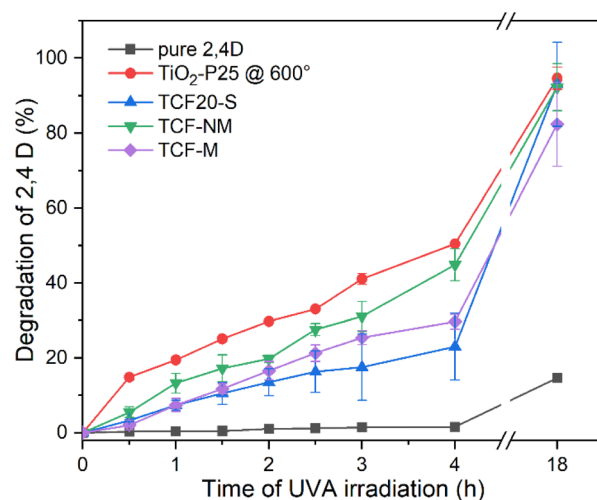

Fig. 7 Photocatalytic degradation of 2,4-D in aqueous solution over time under UVA irradiation by various photocatalytic materials: TCF20-S, TCF-M, TCF-NM and TiO$_2$ 600 °C. In addition, the degradation of a pure 2,4-D aqueous solution is shown.

complete mineralisation into carbon dioxide, water, and gaseous products[60–62]

Photodegradation of 2,4-D by pure TiO_2-P25 was not assessed due to opacity of the respective suspension but TiO_2-P25 @ 600 °C demonstrated the highest degradation rate across all materials, achieving 20% loss of 2,4 D within 1 h, 40% loss of 2,4 D within 3 h and nearly complete degradation of 2,4-D (around 94.6%) after 18 h (Fig. 7). Within the first 1.5 hours of UVA irradiation, both TCF20-S and TCF-M materials exhibited comparable degradation rates. After this time frame, magnetically extracted TCF-M material showed a higher rate of degradation, achieving 26% of 2,4-D degradation by 3 hours, whereas the TCF20-S reached a slightly lower level of degradation by the same time. TCF-NM material demonstrated relatively good results, degrading 16% of 2,4 D within 1 h and 30% of 2,4 D degradation within 3 h and nearly complete degradation of 2,4-D (around 93%) after 18 hours.

The superior photocatalytic activity of pure TiO_2-P25 @ 600 °C when compared with TCF20-S, TCF-M, and TCF-NM materials can be attributed to its relatively higher anatase content while in the case of the latter TiO_2 has mostly rutile crystal structure (see Table 1). Therefore, from photocatalytic activity results it is clear that the photocatalytic component in the synthesized materials is TiO_2 and $CuFe_2O_4$–Fe_2O_3 works as a magnetic addition. TCF-M exhibits lower photocatalytic activity as it contains 20% less photocatalytic material than pure TiO_2-P25 @ 600 °C.

Despite the higher degradation rate of pure TiO_2-P25 @ 600 °C and TCF-NM compared with TCF-M, their very fine size (less than 100 nm, even in size of tens of nm) and non-magnetic nature presents challenges for low-cost recovery and recycling. Therefore, despite its relatively lower photocatalytic activity, the magnetic properties of TCF-M can be used to easily collect this material from the environment and repeatedly used as photocatalyst material. In Fig. 8 the photocatalytic activity of TCF-M after five cycles (use and magnetic extraction) is

demonstrated. Only a slight decrease in the photocatalytic degradation rate through subsequent cycles was observed while the photocatalytic efficiency of this material remains commendably high. This stability of photocatalytic and 2,4-D degrading activity of TCF-M material after repeated use and collection from water strongly recommends the potential of this material as a reliable and practical choice for water purification applications, including recyclability.

4 Conclusions

In the present study we propose a sintered mixture of TiO_2-P25 and $CuFe_2O_4$–Fe_2O_3 to obtain a magnetically collectable photocatalyst. $CuFe_2O_4$–Fe_2O_3 material was synthesized using co-precipitation method. The obtained material was then mechanically mixed with TiO_2-P25 and annealed at 600 °C to form a photocatalytic material (TCF20-S). TCF20-S material was further separated to magnetically collectable part (TCF-M) and non-magnetic residue (TCF-NM) and properties and performance of those fractions were compared. Additionally, we extended our analysis to TCF-M material that had been re-used over 5 cycles (TCF-M-5c), to assess its durability and sustained photocatalytic activity.

The synthesized materials had fine grain sizes ranging from 20 to several hundreds nanometers. Elemental distribution of TCF-M demonstrated heterogeneously dispersed nanoscopic Fe and uniformly distributed Cu particles. Elemental composition measured with ICP-OES aligned closely with our initial synthetic expectations and confirmed that the TCF-M sample had a balanced Ti/Fe atomic ratio indicating the effective incorporation of TiO_2 into the magnetic fraction. The XRD patterns of TCF20-S, TCF-NM, TCF-M and TCF-M-5c showed the presence of rutile, anatase, hematite (α-Fe_2O_3), $CuFe_2O_4$ spinel and maghemite (γ-Fe_2O_3). According to XPS and NEXAFS, titanium was in Ti^{4+}, copper was predominantly in Cu^{2+} and iron was mainly in Fe^{3+} state in all materials. All materials involving TiO_2, exhibited intense absorption in the UVA spectrum, but in case of TCF20-S, TCF-NM, TCF-M and TCF-M-5c also absorption in the visible light spectrum was observed. The latter was due to the presence of Fe_2O_3 and $CuFe_2O_4$ in material, which have absorption in the visible range. The saturation magnetic moment at room temperature is consistent with the calculated magnetisation of all crystal phases present and temperature dependence of magnetisation reveals magnetic transition temperatures that are expected for given phase composition. Improved magnetic properties make studied mixtures well suitable for magnetic collection in water treatment processes.

Photocatalytic activity of materials was evaluated as degradation of the model herbicide pollutant 2,4-D under UVA. Out of all the tested materials pure TiO_2-P25 @ 600 °C exhibited the highest photocatalytic activity, which was due to its predominant anatase content in the crystal phase. TCF-NM, TCF20-S and TCF-M materials showed lower photocatalytic activity than TiO_2-P25 @ 600 likely due to the relatively higher presence of rutile phase combined with general lower TiO_2 content. However, while TiO_2-P25 @ 600 °C can not be recycled from water after photocatalytic reaction due to its fine gram size,
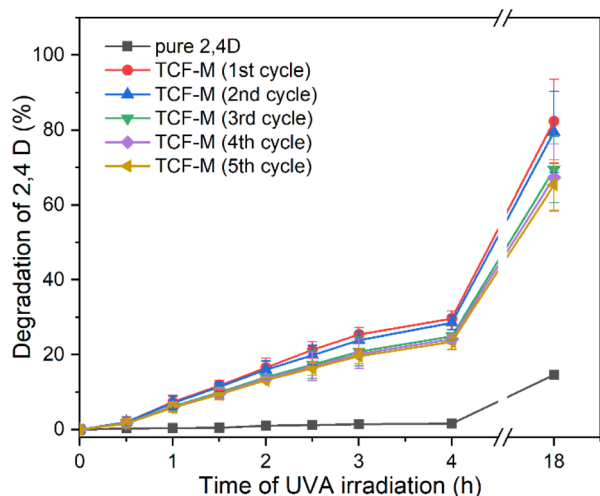

Fig. 8 Time-dependent photocatalytic degradation of 2,4-D in aqueous solution using TCF-M, under UVA irradiation, after five cycles of use. For comparison, the degradation trend of a pure 2,4-D aqueous solution is also depicted.

TCF-M shows a potency for easy removal due to its magnetic properties. The latter was proven by 5 cycles of use, collection and reuse of the material. Therefore, we see a remarkable potential for this material in water purification.

Author contributions

Dmytro Danilian: investigation, validation, formal analysis, visualization, data curation, methodology, conceptualization, writing – original draft. Franziska Maria Bundrück: investigation, formal analysis. Arvo Kikas: investigation, formal analysis. Tanel Käämbre: investigation, formal analysis, writing – review & editing. Hugo Mändar: investigation, formal analysis, resources, visualization, writing – review & editing. Sandro Lehner: investigation. Alexander Gogos: investigation, formal analysis, resources, visualization, writing – review & editing. Jekaterina Kozlova: investigation, formal analysis, visualization. Mati Kook investigation, formal analysis. Valter Kiisk: formal analysis, resources. Joosep Link: investigation, formal analysis, visualization. Raivo Stern: investigation, formal analysis, resources, funding acquisition. Angela Ivask: writing – review & editing, funding acquisition, supervision. Vambola Kisand: writing – review & editing, funding acquisition, resources, supervision. Rainer Pärna: conceptualization, methodology, formal analysis, writing – review & editing, resources, funding acquisition, supervision, project administration.

Conflicts of interest

The authors declare that they have no known competing financial interests or personal relationships that could have appeared to influence the work reported in this paper.

Acknowledgements

References

1 M. Syafrudin, R. A. Kristanti, A. Yuniarto, T. Hadibarata, J. Rhee, W. A. Al-onazi, T. S. Algarni, A. H. Almarri and A. M. Al-Mohaimeed, *Int. J. Environ. Res. Public Health*, 2021, **18**, 468.

2 R. Z. Marsala, E. Capri, E. Russo, M. Bisagni, R. Colla, L. Lucini, A. Gallo and N. A. Suciu, *Sci. Total Environ.*, 2020, **736**, 139730.

3 Ü. Leisk and R. Rebane, *Taimekaitsevahendite Jääkide Sisalduse Ja Dünaamika Uuring Pinna- Ja Põhjavees*, Estonian Environmental Research Centre, 2018.

4 V. Kõrgmaa, E. Usin, Ü. Leisk, M. Laht, V. Värk, S. Otsmaa, K. Pachel, J. Jaaku, M. Kriipsalu, K. Pehme, I. Tamm, L. Albreht, M. Lukk, L. Liepkalns, A. Marandi, J. Pärn, V. Raidla and K. Vooro, *Hajaasustuspiirkondade Joogivee Kvaliteedi Ja -süsteemide Uuring*, Eesti Keskkonnauuringute Keskus OÜ, 2020.

5 F. H. M. Tang, M. Lenzen, A. McBratney and F. Maggi, *Nat. Geosci.*, 2021, **14**, 206–210.

6 A. F. Gilca, C. Teodosiu, S. Fiore and C. P. Musteret, *Chemosphere*, 2020, **259**, 127476.

7 V. K. Gupta and I. Ali, *Environmental Water*, 2013, pp. 1–27.

8 G. Ren, H. Han, Y. Wang, S. Liu, J. Zhao, X. Meng and Z. Li, *Nanomaterials*, 2021, **11**, 1804.

9 H. He, Z. Luo and C. Yu, *J. Alloys Compd.*, 2020, **816**, 152652.

10 H. He, Z. Luo and C. Yu, *Colloids Surf., A*, 2021, **613**, 126099.

11 H. He, Z. Luo, Z.-Y. Tang and C. Yu, *Appl. Surf. Sci.*, 2019, **490**, 460–468.

12 F. Yi, J. Ma, C. Lin, H. Zhang, Y. Qian, H. Jin and K. Zhang, *Chem. Eng. J.*, 2022, **427**, 132028.

13 S. Anandan, Y. Ikuma and K. Niwa, *Solid State Phenom.*, 2010, **162**, 239–260.

14 F. Yi, J. Ma, C. Lin, L. Wang, H. Zhang, Y. Qian and K. Zhang, *J. Alloys Compd.*, 2020, **821**, 153557.

15 H. He, J. Jiang, Z. Luo, D. Li, M. Shi, H. Sun, J. Chen, C. Chen, B. Deng and C. Yu, *Colloids Surf., A*, 2023, **667**, 131357.

16 Z. Xu, Y. Ren, X. Deng, M. Xu, W. Chai, X. Qian and Z. Bian, *Adv. Energy Sustainability Res.*, 2022, **3**(11), 2200105.

17 V. Kisand, U. Joost, V. Reedo, R. Pärna, T. Tätte, J. Shulga, A. Saar, L. Matisen, A. Kikas and I. Kink, *Appl. Surf. Sci.*, 2010, **256**, 4538–4542.

18 Q. Guo, C. Zhou, Z. Ma and X. Yang, *Adv. Mater.*, 2019, **31**, e1901997.

19 M. Mishra and D.-M. Chun, *Appl. Catal., A*, 2015, **498**, 126–141.

20 R. M. Cornell and U. Schwertmann, *The Iron Oxides*, 2003.

21 M. R. A. Kumar, B. Abebe, H. P. Nagaswarupa, H. C. A. Murthy, C. R. Ravikumar and F. K. Sabir, *Sci. Rep.*, 2020, **10**, 1249.

22 W. Bootluck, T. Chittrakarn, K. Techato and W. Khongnakorn, *J. Environ. Chem. Eng.*, 2021, **9**, 105660.

23 R. S. Yadav, J. Havlica, J. Masilko, L. Kalina, J. Wasserbauer, M. Hajdúchová, V. Enev, I. Kuřitka and Z. Kožáková, *J. Supercond. Novel Magn.*, 2016, **29**, 759–769.

24 S. P. Kamble, S. P. Deosarkar, S. B. Sawant, J. A. Moulijn and V. G. Pangarkar, *Ind. Eng. Chem. Res.*, 2004, **43**, 8178–8187.

25 N. Fairley, V. Fernandez, M. Richard-Plouet, C. Guillot-Deudon, J. Walton, E. Smith, D. Flahaut, M. Greiner, M. Biesinger, S. Tougaard, D. Morgan and J. Baltrusaitis, *Appl. Surf. Sci. Adv.*, 2021, **5**, 100112.

26 R. Pärna, R. Sankari, E. Kukk, E. Nõmmiste, M. Valden, M. Lastusaari, K. Kooser, K. Kokko, M. Hirsimäki, S. Urpelainen, P. Turunen, A. Kivimäki, V. Pankratov, L. Reisberg, F. Hennies, H. Tarawneh, R. Nyholm and M. Huttula, *Nucl. Instrum. Methods Phys. Res., Sect. A*, 2017, **859**, 83–89.

27 W. Wang, A. Kivimäki, K. Chernenko, R. Pärna, T. Käämbre, E. Kukk, K. Kokko, M. Valden, M. Hirsimäki, M. Kirm and M. Huttula, *J. Phys.: Conf. Ser.*, 2022, **2380**, 012048.

28 M. Kumar, M. N. Islam, F. L. Terry, M. J. Freeman, A. Chan, M. Neelakandan and T. Manzur, *Appl. Opt.*, 2012, **51**, 2794.

29 *QD Application Note 1500-021 Rev. B0*, 2020.

30 M. M. Viana, V. F. Soares and N. D. S. Mohallem, *Ceram. Int.*, 2010, **36**, 2047–2053.

31 D. A. H. Hanaor and C. C. Sorrell, *J. Mater. Sci.*, 2011, **46**, 855–874.

32 T. Ohsaka, F. Izumi and Y. Fujiki, *J. Raman Spectrosc.*, 1978, **7**, 321–324.

33 R. Liang, A. Hu, W. Li and Y. N. Zhou, *J. Nanopart. Res.*, 2013, **15**, 1990.

34 Lj. D. Arsov, C. Kormann and W. Plieth, *J. Raman Spectrosc.*, 1991, **22**, 573–575.

35 S. P. Schwaminger, P. Fraga-García, F. Selbach, F. G. Hein, E. C. Fuß, R. Surya, H.-C. Roth, S. A. Blank-Shim, F. E. Wagner, S. Heissler and S. Berensmeier, *Adsorption*, 2017, **23**, 281–292.

36 L. S. Mdletshe, P. R. Makgwane and S. S. Ray, *Nanomaterials*, 2019, **9**, 1140.

37 S. Challagulla, K. Tarafder, R. Ganesan and S. Roy, *Sci. Rep.*, 2017, **7**, 8783.

38 B. H. Toby, *Powder Diffr.*, 2006, **21**, 67–70.

39 E. McCafferty and J. P. Wightman, *Surf. Interface Anal.*, 1998, **26**, 549–564.

40 J. J. Yeh and I. Lindau, *At. Data Nucl. Data Tables*, 1985, **32**, 1–155.

41 T. Yamashita and P. Hayes, *Appl. Surf. Sci.*, 2008, **254**, 2441–2449.

42 Q. Qin, Y. Liu, X. Li, T. Sun and Y. Xu, *RSC Adv.*, 2018, **8**, 1071–1077.

43 H. He, J. Xiao, Z. Liu, B. Yang, D. Wang, X. Peng, L. Zeng, Z. Li, L. Lei, M. Qiu and Y. Hou, *Chem. Eng. J.*, 2023, **453**, 139751.

44 J. F. Moulder, W. F. Stickle, P. E. Sobol and K. D. Bomben, *Handbook of X-Ray Photoelectron Spectroscopy*, Perkim-Elmer Corporation, Eden Prairie, 1992.

45 G. van der Laan, C. Westra, C. Haas and G. A. Sawatzky, *Phys. Rev. B: Condens. Matter Mater. Phys.*, 1981, **23**, 4369–4380.

46 H. He, L. Zeng, X. Peng, Z. Liu, D. Wang, B. Yang, Z. Li, L. Lei, S. Wang and Y. Hou, *Chem. Eng. J.*, 2023, **451**, 138628.

47 L. Trotochaud, A. R. Head, S. Pletincx, O. Karslıoğlu, Y. Yu, A. Waldner, L. Kyhl, T. Hauffman, H. Terryn, B. Eichhorn and H. Bluhm, *J. Phys. Chem. B*, 2018, **122**, 1000–1008.

48 Z. Li, J. Lyu and M. Ge, *J. Mater. Sci.*, 2018, **53**, 15081–15095.

49 S. Tanuma, C. J. Powell and D. R. Penn, *Surf. Interface Anal.*, 1994, **21**, 165–176.

50 J. Stöhr, *NEXAFS Spectroscopy*, Springer, Berlin, Heidelberg, 2017.

51 C. C. Chusuei, M. A. Brookshier and D. W. Goodman, *Langmuir*, 1999, **15**, 2806–2808.

52 X. Wang, S. O. Pehkonen, J. Rämö, M. Väänänen, J. G. Highfield and K. Laasonen, *Catal. Sci. Technol.*, 2011, **2**, 784–793.

53 A. Meidanchi and H. Ansari, *J. Cluster Sci.*, 2021, **32**, 657–663.

54 P. Makuła, M. Pacia and W. Macyk, *J. Phys. Chem. Lett.*, 2018, **9**, 6814–6817.

55 B. D. Cullity and C. D. Graham, *Introduction to Magnetic Materials*, IEEE Press, 2008.

56 C. Xia, Y. Jia, M. Tao and Q. Zhang, *Phys. Lett. A*, 2013, **377**, 1943–1947.

57 S. Piccinin, *Phys. Chem. Chem. Phys.*, 2019, **21**, 2957–2967.

58 A. U. Gehring, H. Fischer, M. Louvel, K. Kunze and P. G. Weidler, *Geophys. J. Int.*, 2009, **179**, 1361–1371.

59 M. I. Dar and S. A. Shivashankar, *RSC Adv.*, 2013, **4**, 4105–4113.

60 F. Amiri, M. Dehghani, Z. Amiri, S. Yousefinejad and A. Azhdarpoor, *Water Sci. Technol.*, 2021, **83**, 3110–3122.

61 S. S, K. L. Nagashree, T. Maiyalagan and G. Keerthiga, *Appl. Surf. Sci.*, 2018, **449**, 371–379.

62 M. Abdennouri, A. Elhalil, M. Farnane, H. Tounsadi, F. Z. Mahjoubi, R. Elmoubarki, M. Sadiq, L. Khamar, A. Galadi, M. Baâlala, M. Bensitel, Y. E. Hafiane, A. Smith and N. Barka, *J. Saudi Chem. Soc.*, 2015, **19**, 485–493.